

Journal of Biomedical Optics

SPIEDigitalLibrary.org/jbo

Thin-film tunable filters for hyperspectral fluorescence microscopy

Peter Favreau
Clarissa Hernandez
Ashley Stringfellow Lindsey
Diego F. Alvarez
Thomas Rich
Prashant Prabhat
Silas J. Leavesley



SPIE

Thin-film tunable filters for hyperspectral fluorescence microscopy

Peter Favreau,^{a,d} Clarissa Hernandez,^a Ashley Stringfellow Lindsey,^b Diego F. Alvarez,^{b,c,d} Thomas Rich,^{b,d} Prashant Prabhat,^e and Silas J. Leavesley^{a,b,d}

^aUniversity of South Alabama, Department of Chemical and Biomolecular Engineering, Mobile, Alabama 36688

^bUniversity of South Alabama, Department of Pharmacology, Mobile, Alabama 36688

^cUniversity of South Alabama, Department of Internal Medicine, Mobile, Alabama 36688

^dUniversity of South Alabama, Center for Lung Biology, Mobile, Alabama 36688

^eSemrock, Inc. (A Unit of IDEX Corporation), 3625 Buffalo Road, Rochester, New York 14624

Abstract. Hyperspectral imaging is a powerful tool that acquires data from many spectral bands, forming a contiguous spectrum. Hyperspectral imaging was originally developed for remote sensing applications; however, hyperspectral techniques have since been applied to biological fluorescence imaging applications, such as fluorescence microscopy and small animal fluorescence imaging. The spectral filtering method largely determines the sensitivity and specificity of any hyperspectral imaging system. There are several types of spectral filtering hardware available for microscopy systems, most commonly acousto-optic tunable filters (AOTFs) and liquid crystal tunable filters (LCTFs). These filtering technologies have advantages and disadvantages. Here, we present a novel tunable filter for hyperspectral imaging—the thin-film tunable filter (TFTF). The TFTF presents several advantages over AOTFs and LCTFs, most notably, a high percentage transmission and a high out-of-band optical density (OD). We present a comparison of a TFTF-based hyperspectral microscopy system and a commercially available AOTF-based system. We have characterized the light transmission, wavelength calibration, and OD of both systems, and have then evaluated the capability of each system for discriminating between green fluorescent protein and highly autofluorescent lung tissue. Our results suggest that TFTFs are an alternative approach for hyperspectral filtering that offers improved transmission and out-of-band blocking. These characteristics make TFTFs well suited for other biomedical imaging devices, such as ophthalmoscopes or endoscopes. © 2014 Society of Photo-Optical Instrumentation Engineers (SPIE) [DOI: [10.1117/1.JBO.19.1.011017](https://doi.org/10.1117/1.JBO.19.1.011017)]

Keywords: hyperspectral imaging; spectral imaging; microscopy; acousto-optic tunable filter; thin-film tunable filter; VersaChrome.

Paper 130126PSSRR received Mar. 7, 2013; revised manuscript received Aug. 27, 2013; accepted for publication Aug. 28, 2013; published online Sep. 26, 2013.

1 Introduction

1.1 Hyperspectral Imaging with Tunable Filters

Fluorescence imaging is a powerful technique that can identify fluorescent labels (fluorophores) in a variety of biological applications, including *in vivo* imaging,^{1,2} fluorescent protein- and quantum dot-tracking,^{3–6} and clinical imaging.^{7–10} Traditional fluorescence microscopy approaches can detect one-to-several spectral bands using bandpass filters with center wavelengths (CWLs) corresponding to peak emission wavelengths of specific fluorophores. Consequently, traditional fluorescence microscopy is effective for identifying fluorescent labels in samples containing one-to-several fluorophores whose peak emission or excitation wavelengths are spectrally distinct. However, many biomedical applications require identification of multiple fluorescent labels with overlapping spectra or separation of labels from tissue autofluorescence, which often has a broad spectral emission that overlaps common labels such as green fluorescent protein (GFP). Although approaches such as fluorescence lifetime microscopy are capable of differentiating overlapping emission peaks based on differences in the fluorescence

lifetime,^{11–13} these approaches are often difficult to implement and relatively expensive. In addition, fluorescence lifetime has been shown to be sensitive to environmental conditions, such as changes in the local refractive index, that could affect measurement accuracy in heterogeneous samples.¹⁴

Recently, hyperspectral imaging techniques from the remote sensing field have been applied to fluorescence microscopy.¹⁵ Hyperspectral fluorescence microscopy permits signal collection over many spectral bands, producing a contiguous spectrum.^{3,16} Hyperspectral fluorescence imaging has resulted in enhanced spectral discrimination for separation of exogenous fluorophores from tissue autofluorescence,^{3,17} measuring fluorescence resonance energy transfer (FRET) efficiency,^{18–20} and live-cell imaging.^{21,22}

The spectral filter is a key component of a hyperspectral imaging system. Unlike traditional fluorescence microscopy, hyperspectral microscopy systems have utilized a variety of spectral filtering technologies, including gratings,^{23,24} prisms,^{25,26} and tunable filters.^{3,7,27,28} Garini et al. and Lerner et al. offer overviews of many commercially available filtering technologies.^{16,29} A traditional spectrometer could also be employed for hyperspectral imaging, if operated in a raster-scanning mode. However, the high light loss would result in acquisition times that are prohibitively long, resulting in photobleaching.

Address all correspondence to: Silas J. Leavesley, University of South Alabama, Department of Chemical and Biomolecular Engineering, 150 Jaguar Dr., SH 4129, Mobile, Alabama 36688. Tel: (251) 460-6160; Fax: (251) 460-1485; E-mail: leavesley@southalabama.edu

Confocal microscope systems have sought to overcome this limitation through the use of multianode photomultiplier tube arrays. For wide-field imaging systems, tunable filters offer a suitable compromise between spectral bandwidths and acquisition time. Common tunable filter technologies include liquid crystal tunable filters (LCTFs)^{4,27} and acousto-optic tunable filters (AOTF).^{3,7,28,30} Several factors that are important for spectral filtering include percent transmission, wavelength tuning range, tuning speed, bandwidth, out-of-band blocking power, and cost. In general, AOTFs offer very fast wavelength switching speed (10 to 30 μ s) but poor light transmission and high cost, whereas LCTFs offer a wide wavelength tuning range but slower wavelength tuning speed and poor light transmission. Both AOTFs and LCTFs have relatively limited out-of-band blocking (OD 3–4) and are often supplemented by additional longpass filters to prevent excitation–emission cross-talk. Consequently, a spectral filter technology that offers high percent transmission, high out-of-band blocking power, and a wide wavelength tuning range at a low cost would greatly increase the ability to perform high-sensitivity, high dynamic range, hyperspectral microscopy studies.

1.2 Thin-Film Tunable Filters for Hyperspectral Imaging

Thin-film optical filters offer many characteristics that are ideal for spectral filtering, such as high optical transmission (>90%), sharp edge cut-offs, and out-of-band optical densities (OD) of 6 or greater. However, traditional thin-film filters have fixed bandpass wavelengths and are not well suited for hyperspectral imaging applications. Here, we present an alternative approach for spectral filtering using tunable thin-film filters. Thin-film technology has previously been used for fixed bandpass microscopy components such as dichroic mirrors and interference filters.³¹ Thin-film tunable filters (TFTF), by contrast, allow variation of the CWL of the passband over a range of wavelengths. Wavelength tuning is achieved by varying the angle of incidence (AOI).

We have previously demonstrated that AOTF-based hyperspectral microscopy can identify GFP-expressing cells in the lung with high sensitivity and specificity.³ In this work, we present results from a novel TFTF-based system with a side-by-side comparison to an AOTF-based system. The optical properties of both systems as well as the capability of both systems to differentiate GFP from lung autofluorescence are presented. Our results indicate that TFTFs offer an alternative hyperspectral filtering approach with high transmission and out-of-band rejection. This filtering approach may be ideal for discriminating weak fluorescence signals from surrounding autofluorescence.

2 Methods

2.1 Cell, Animal, and Sample Preparation

All animal work was approved by our Institutional Animal Care and Use Committee and conforms to standard practices and established guidelines. Highly proliferative pulmonary microvascular endothelial cells (PMVECs) were isolated and transduced with a lentivirus-encoding GFP as described previously.^{3,32} Adult male CD rats were infected intratracheally with *Pseudomonas aeruginosa* and then injected with 10^6 cells/100g of body weight GFP-positive PMVECs in the jugular vein. Rats not

injected with GFP-positive PMVECs were injected with saline and used as autofluorescence controls. One week post-injection, animals were euthanized and lungs were removed and ventilated at a constant volume of 7 mL/kg. The most injured portion of the lung was excised and immersion fixed in formalin for 24 h. Tissues were then embedded in paraffin, cut into 10- μ m slices and placed on microscope slides for imaging. Slides were deparaffinized using treatments of xylene and 70% ethanol. Slides containing tissue with GFP-positive PMVECs were stained with 10 μ L of 0.225 μ M Hoechst-33342 (Life Technologies, Carlsbad, California). Slides were also prepared using tissue from negative control rats. These tissues were not labeled with Hoechst. Fluorescence mounting medium (Dako, North America, Inc., Carpinteria, California) was used for slide preparation.

Samples of GFP-positive PMVECs were prepared as confluent monolayers on a 25-mm-round coverslip and were used as controls for the pure GFP spectrum. Confluent monolayers of wild-type PMVECs on 25-mm-round coverslip were labeled with 10 μ L of 0.225 μ M Hoechst-33342 and used as controls for the pure Hoechst spectrum.

2.2 Hyperspectral Microscope Set-Up, Calibration, and Spectral Correction

All imaging was performed using an inverted fluorescence microscope (TE2000-U, Nikon Instruments, Melville, New York), equipped with a 40 \times -oil immersion objective (S Fluor, 40 \times /1.30 Oil DIC H/N2, Nikon Instruments). Figure 1 shows the complete wide-field fluorescence microscope with attached hyperspectral filtering modules. A Xe arc lamp (Lambda DG-4, Sutter Instruments, Novato, California) provided excitation light. A 360/40-nm filter (D360/40X, Chroma Technology Corp., Bellows Falls, Vermont) was used for Hoechst excitation. GFP and autofluorescence were excited using a 430/24-nm filter (ET430/24X, Chroma Technology Corp.). A custom fluorescence filter cube consisting of a longpass dichroic beamsplitter (FF-458-Di02, Semrock, Inc., Rochester, New York) and longpass fluorescence emission filter (BLP01-458R, Semrock, Inc.) was utilized to separate emission from excitation light. Hyperspectral imaging was accomplished for each sample, using each type of tunable filter, by acquiring

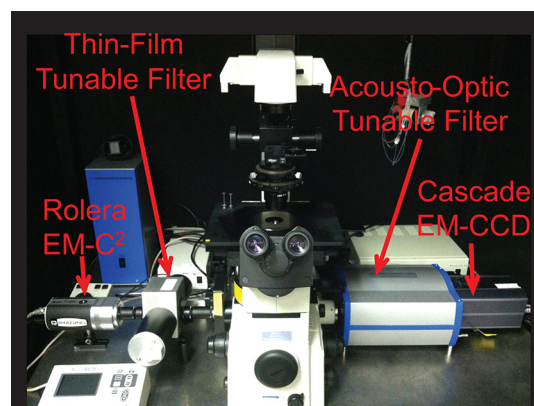


Fig. 1 Custom wide-field fluorescence microscope used for image acquisition. The fluorescence emission was scanned from 470 to 700 nm using either a thin-film tunable filter (TFTF) system or an acousto-optic tunable filter (AOTF) system. Fluorescence images were collected using charge-coupled device (CCD) cameras, permitting image acquisition of the same field of view for both filtering technologies.

an image stack over a wavelength range of 470 to 700 nm, in 5-nm increments. The right camera port of the microscope was connected to a previously tested AOTF (HSi-300, ChromoDynamics, Inc., Lakewood, New Jersey).³ A charge-coupled device (CCD) camera was used for image acquisition (Cascade 512B, Photometrics, Tucson, Arizona). The Cascade 512B and AOTF were controlled using μ Manager software (Vale Lab, UCSF).

2.2.1 Fresco™ TFTF system

A modular TFTF system (Fresco™ tunable filter system, an internal product by Semrock Inc., a Unit of IDEX) was developed to house an array of TFTFs. Each TFTF (VersaChrome®,

Semrock, Inc.) in the array has between 15- and 20-nm bandwidth [full-width at half-maximum (FWHM)] and a tuning range of >12% of the normal-incidence wavelength, which corresponds to 40 to 85 nm of tuning range for the selected filters (see Table 1). Unlike standard thin-film interference filters, the transmission spectrum of TFTF filters can be angle tuned (i.e., the transmission spectrum changes as a function of AOI) without exhibiting significant change in the shape of the spectrum, the percent transmission, or the out-of-band rejection. This is illustrated for a 628 nm, at 0 deg AOI, filter (Fig. 2). As the CWL of this filter is angle tuned, the filter retains its bandwidth at higher AOIs as well as a high transmission, steep spectral edges, and high out-of-band rejection. The CWL tunability is continuous over the entire wavelength range.

The CWL of a TFTF is dictated by the following equation:

$$\lambda(\theta) = \lambda(0) \sqrt{1 - \frac{\sin^2(\theta)}{n_{\text{eff}}^2}}, \quad (1)$$

where θ is the AOI and n_{eff} is the “effective index of refraction,” which is unique for each filter design. n_{eff} is a composite measure of refractive index that is a function of the refractive index and thickness of each thin-film layer that comprises a thin-film filter.³³ Although n_{eff} can be estimated theoretically, more accurate tuning characteristics are obtained by measuring the CWL [$\lambda(\theta)$] as a function of AOI (θ) and fitting the resulting data using the above equation. Hence, n_{eff} is assumed to be a constant over the tuning range of the filter ($\theta = 0$ to 60 deg). This characterization is performed during the manufacturing process and is supplied with each VersaChrome filter. The spectral properties of these tunable filters are almost identical for both s and p polarizations of light. Hence, a TFTF-based hyperspectral imaging system can detect both polarizations simultaneously (as opposed to AOTFs or LCTFs, which, generally, can only detect a single polarization).

Part number	Center Wavelength range (nm)	Bandwidth (nm)	Effective Index of refraction
TBP01-451-15	398.4–451.6	16.6	1.84
TBP01-503-15	447.5–504.2	21.6	1.88
TBP01-564-14	497.6–563.0	21.2	1.85
TBP01-632-14	557.5–630.8	17.9	1.85
TBP01-708-13	624.2–710.0	21.5	1.82

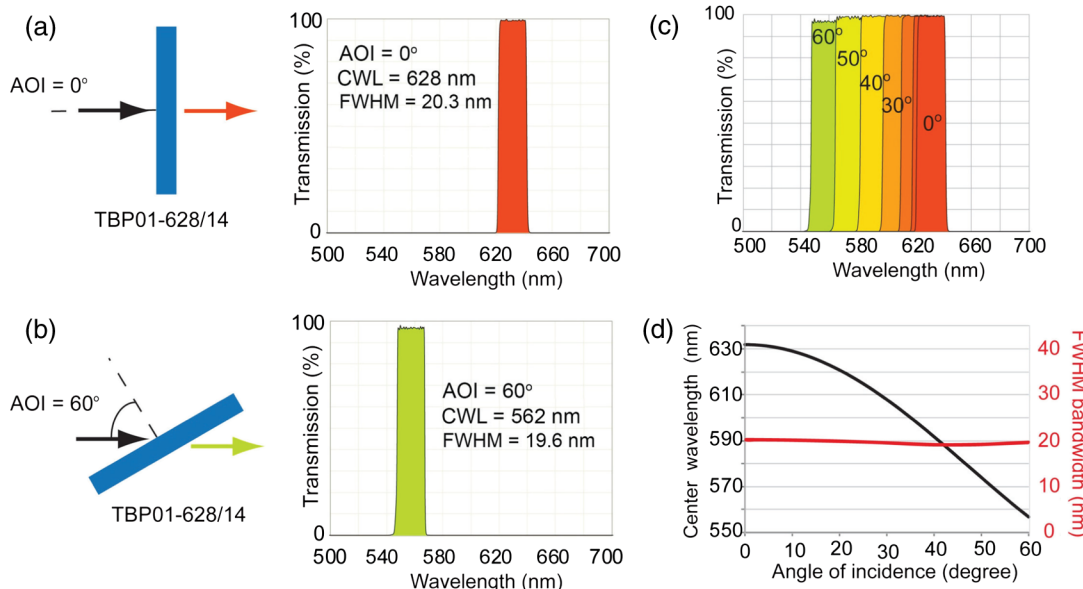


Fig. 2 A TFTF (VersaChrome, Semrock, Inc.) allows the center wavelength (CWL) of the pass-band to be tuned by varying the angle of incidence (AOI). The same filter produces different transmission spectra at 0 deg AOI (a) and at 60 deg AOI (b). The CWL of this filter can be continuously tuned over its entire range by changing the AOI of the filter. Representative transmission spectra, in 10 deg increments, are shown (c) and the angle-tuned CWL is plotted (d, black solid line). The full-width at half-maximum (FWHM) bandwidth of this filter remains virtually constant (d, red line). All plots were generated for a 628 nm, at 0 deg AOI, TFTF (TBP01-632-14, Semrock, Inc.).

2.2.2 Hyperspectral filter module using TFTFs

The filtering system developed for this study can accommodate up to six filters in a filter array, although devices with alternative numbers of filters could also be designed. Our implementation included five VersaChrome TFTF filters and one empty filter slot, which allowed scanning over the full visible range (400 to 700 nm) as well as detection of unfiltered transmission (for transmitted light imaging). Additional details about the filters used in our experiments are available in Table 1. The TFTF unit was computer controlled using FilterPalette™ software (an internal product by Semrock, Inc.). A series of coefficients was stored for each filter, and Eq. 1 was used to allow wavelength tuning over the range of each filter. Using all five filters sequentially, wavelength tuning from 400 to 700 nm was possible. In order to generate this spectral data, measured transmission spectra of VersaChrome filters were obtained (at Semrock) at 0 and 60 deg AOI following standard spectral measurement procedures. When a CWL is specified, FilterPalette automatically selects the appropriate VersaChrome filter and rotates it to the correct angle.

A CCD camera was used with the TFTF system for image acquisition (Rolera EM-C², QImaging). The TFTF and AOTF systems were aligned to allow imaging of the same field of view. The Rolera EM-C² was controlled using NIS Elements (NIS Elements 3.2, Nikon Instruments, Inc.) software. Wavelength switching and image acquisition were synchronized using external, transistor-transistor logic triggering.

2.2.3 Filter characterization and wavelength calibration

The AOTF and TFTF systems were characterized using a fiber-coupled USB spectrometer (QE6500, Ocean Optics, Inc., Dunedin, Florida). The bright-field (transmitted light) lamp was used as the light source for measuring filter transmission. The microscope was brought into focus using a blank slide. The fiber from the spectrometer was connected directly to the microscope (without any tunable filters in the light path) to measure the spectrum of the lamp before entering the tunable filter. A background spectrum was also collected with the light source turned off. The tunable filter was then reattached to the microscope and the filtered spectrum was measured using the USB spectrometer for each wavelength band in the imaging protocol (described above). The background spectrum was subtracted from all measured spectra to correct for stray light. The percent transmission spectrum for each tunable filter, at each tuning CWL, was then calculated.

A multi-ion discharge lamp (MIDL, LightForm, Inc., Asheville, North Carolina) was used to confirm wavelength calibration. The MIDL was placed on the stage. The lamp position was adjusted to fill at least 50% of the dynamic range of the detector for both tunable filter systems when each was tuned to 560 nm CWL. A background spectrum was collected for each hyperspectral filter system. MIDL spectra were then acquired and corrected (as described below) for each hyperspectral filter system.

2.2.4 Spectral correction

Spectral correction was used to compensate for wavelength-dependent attenuation of each hyperspectral system. A dark, or blank, image stack was acquired to account for background signal. For tissue slices, a blank area of the slide was used;

for cultured monolayers, a blank 25-mm-round coverslip with extracellular buffer was used. A bright image stack was then acquired using a National Institute of Science and Technology (NIST)-traceable light source (LS-1-CAL-INT, Ocean Optics, Inc.). The light source was positioned to fill at least 50% of the dynamic range of the detector at 700 nm. Both dark and bright images were taken with identical settings. All measurements were taken using identical settings as the tissue and cell samples for both the AOTF and TFTF systems. A transfer function was then calculated for each system

$$\text{TF}(\lambda) = \frac{I_{\text{Bright}}(\lambda) - I_{\text{Dark}}(\lambda)}{I_{\text{Lamp}}(\lambda)}, \quad (2)$$

where $I_{\text{Bright}}(\lambda)$ and $I_{\text{Dark}}(\lambda)$ represent the average intensity of the bright and dark images, respectively, and $I_{\text{Lamp}}(\lambda)$ represents the known NIST-traceable lamp spectrum at each CWL, λ . A correction coefficient (CC) was calculated as the inverse of the transfer function

$$\text{CC}(\lambda) = \frac{1}{\text{TF}(\lambda)} = \frac{I_{\text{Lamp}}(\lambda)}{I_{\text{Bright}}(\lambda) - I_{\text{Dark}}(\lambda)}. \quad (3)$$

All hyperspectral image data were corrected by subtracting the dark spectrum from the raw image data and by multiplying the CC. A new dark spectrum was acquired for each sample. All correction calculations were performed using MATLAB software (MATLAB R2012b, MathWorks, Natick, Massachusetts).

2.3 Image Acquisition

Hyperspectral image stacks of fluorescence emission were acquired over a wavelength range of 470 to 700 nm in 5-nm increments, for both filter systems. An acquisition time of 500 ms and EMCCD gain at 3800 were used for both systems, for all samples. The total spectral image acquisition time required for the AOTF system was ~30 s, whereas the acquisition time required for the TFTF was ~126 s. It should be noted that the mechanical rotation and translation hardware for the TFTF system could be altered to allow for higher speed switching in future prototypes. For each field-of-view, a spectral scan was performed with 430-nm excitation (for identifying autofluorescence and GFP). A separate image was acquired with 360-nm excitation and 480-nm emission for identifying Hoechst. An image stack was acquired in a region of the slide containing no tissue to determine the background spectrum of the slide. Background subtraction and flat-field correction were performed for all samples using appropriate dark regions for each slide.

2.4 Image Analysis

The bit-depth of both detectors was linearly scaled to fill 16-bit space to allow accurate intensity comparisons. A separate spectral library was constructed for both hyperspectral systems. ENVI software (ENVI 5, Exelis Visual Information Solutions) was used for linear unmixing and image analysis, and Excel (Office 2010, Microsoft) was used for plotting and organizing spectral data. Linear unmixing calculates the abundance of one or many fluorophores in each pixel based on reference spectra stored in a spectral library. Linear unmixing has been shown to be an accurate approach for measuring relative fluorophore concentrations for samples, such as GFP detection¹² and

FRET quantification,²⁰ with minimal nonlinear effects (scattering, etc.). Thus, obtaining a spectral library that accurately represents the spectra of GFP, Hoechst, and lung autofluorescence is required to linearly unmix an image stack.

A monolayer of GFP-expressing PMVECs was used to obtain a pure GFP spectrum. The GFP-containing regions were defined through intensity thresholding at 500 nm. Threshold levels were adjusted to cleanly delineate areas of cell borders. A maximum threshold was also used to exclude over-saturated pixels. A pure Hoechst spectrum was obtained with the same procedure using Hoechst-labeled PMVECs that did not express GFP. Hoechst regions were defined by intensity thresholding at 480 nm. The tissue autofluorescence spectrum was measured by selecting a field-of-view in a slide containing no GFP or Hoechst. Autofluorescence regions were defined by intensity thresholding at 505 nm. The final spectral library for both filter systems contained GFP, Hoechst, and tissue autofluorescence.

The spectral library was used to linearly unmix GFP, Hoechst, and autofluorescence from mixed images. Unmixed images were saved as tiff files and merged into a composite image using NIS Elements software. All images were scaled identically for visual inspection.

3 Results

3.1 Filter Characterization and Wavelength Calibration

The transmission spectra of the AOTF and TFTF systems were measured using a fiber-coupled spectrometer. Both filtering systems were compared at different tuning wavelengths, from 470 to 700 nm in 5-nm increments [Figs. 3(a) and 3(b), selected tuning wavelengths displayed]. The AOTF transmitted 25% of the light from the lamp spectrum and had a bandwidth, as measured

by the FWHM, of 8.5 nm [Fig. 3(a)]. By comparison, the TFTF transmitted 80% to 95% of the lamp spectrum and had a bandwidth of about 20 nm [Fig. 3(b)].

An MIDL was used to test the wavelength calibration and bandwidth of both hyperspectral imaging systems. The MIDL emits a reproducible spectrum with many narrow peaks [Figs. 3(c) and 3(d)]. Image stacks from 470 to 700 nm were acquired using both systems. Each image stack was corrected for flat spectral response. The AOTF system detected the MIDL spectrum with a high degree of spectral similarity (Fig. 3). The TFTF system exhibited a broadening of the characteristic emission peaks of the MIDL lamp [Fig. 3(d)], due to the wider bandwidth of the TFTF. Both systems detected the prominent emission peaks at their correct wavelengths (488, 540, 580, and 610 nm).

3.2 Spectral Correction

Spectral correction was performed for each hyperspectral imaging system to account for wavelength-dependent attenuation and sensitivity. The spectrum of a NIST-traceable lamp [Fig. 4(a)] was measured using the AOTF [Fig. 4(b)] and TFTF [Fig. 4(c)] systems. Both hyperspectral systems reproduced the broad features of the NIST-traceable lamp while adding minor wavelength-dependent artifacts. The background spectrum was also measured for the AOTF [Fig. 4(d)] and TFTF [Fig. 4(e)] systems.

The spectra obtained from the NIST-traceable lamp and the background spectra were used to calculate the spectral transfer function for the AOTF [Fig. 4(f)] and the TFTF [Fig. 4(g)]. Both hyperspectral systems transmitted light more efficiently at higher wavelengths, possibly due to the quantum efficiency of the cameras and variation in filter bandwidths over the spectral range.

The inverse of the transfer function (or CC) is a measure of how light is attenuated through the hyperspectral system. The CC for each hyperspectral system was used to correct for wavelength-dependent attenuation and sensitivity. The CCs for the AOTF [Fig. 4(h)] and TFTF [Fig. 4(i)] were highest at 470 nm and lowest at 700 nm.

3.3 Control Samples and Spectral Libraries

Control samples of GFP-positive PMVECs and Hoechst-labeled wild-type PMVECs were imaged to obtain the pure spectrum of GFP and Hoechst, respectively. An autofluorescence spectrum was obtained from a lung tissue slide containing no GFP or Hoechst. Regions of interest (shown in red) were selected by intensity thresholding the total fluorescence image (sum of all wavelength bands) for the AOTF [Figs. 5(a)–5(c)] and TFTF [Figs. 5(d)–5(f)]. The spectrum for each fluorophore was measured and compiled in a spectral library. The GFP spectrum from the AOTF and TFTF [Fig. 5(g)] was very similar, whereas the Hoechst [Fig. 5(h)] and autofluorescence [Fig. 5(i)] spectra differed slightly between systems. The TFTF produced small spectral “artifacts” at 505, 565, and 625 nm due to mechanical switching of the filters.

3.4 Linear Spectral Unmixing

Slides containing GFP-expressing PMVECs, Hoechst-labeled PMVECs, and autofluorescence were imaged using both hyperspectral systems. A representative image, after correction, is

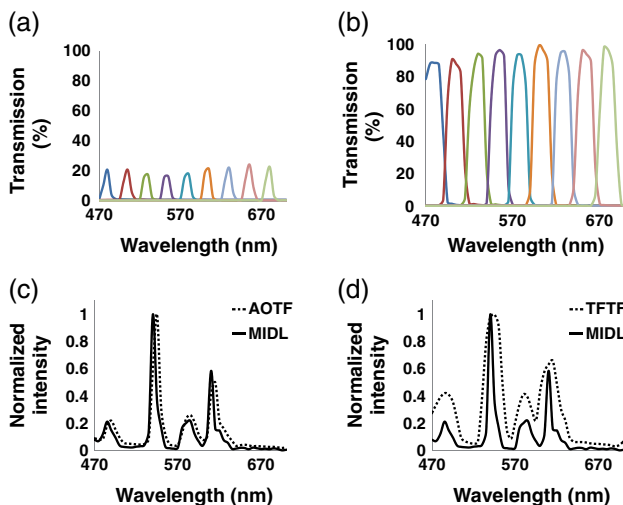


Fig. 3 The AOTF and TFTF were characterized using a fiber-coupled spectrometer (a and b, respectively). Light from the microscope lamp was passed through the AOTF system in one spectral scan (a) and then passed through the TFTF system (b) in a separate spectral scan. A multi-ion discharge lamp (MIDL, Panels c and d—solid line measured using a fiber-coupled spectrometer) was used to assess the wavelength calibration of the AOTF (c) and TFTF (d). MIDL data for each hyperspectral imaging system were collected from hyperspectral image stacks using a wavelength range of 470 to 700 nm and a spectral step size of 5 nm. Optical density plots for the AOTF and TFTF systems are shown in Fig. 9.

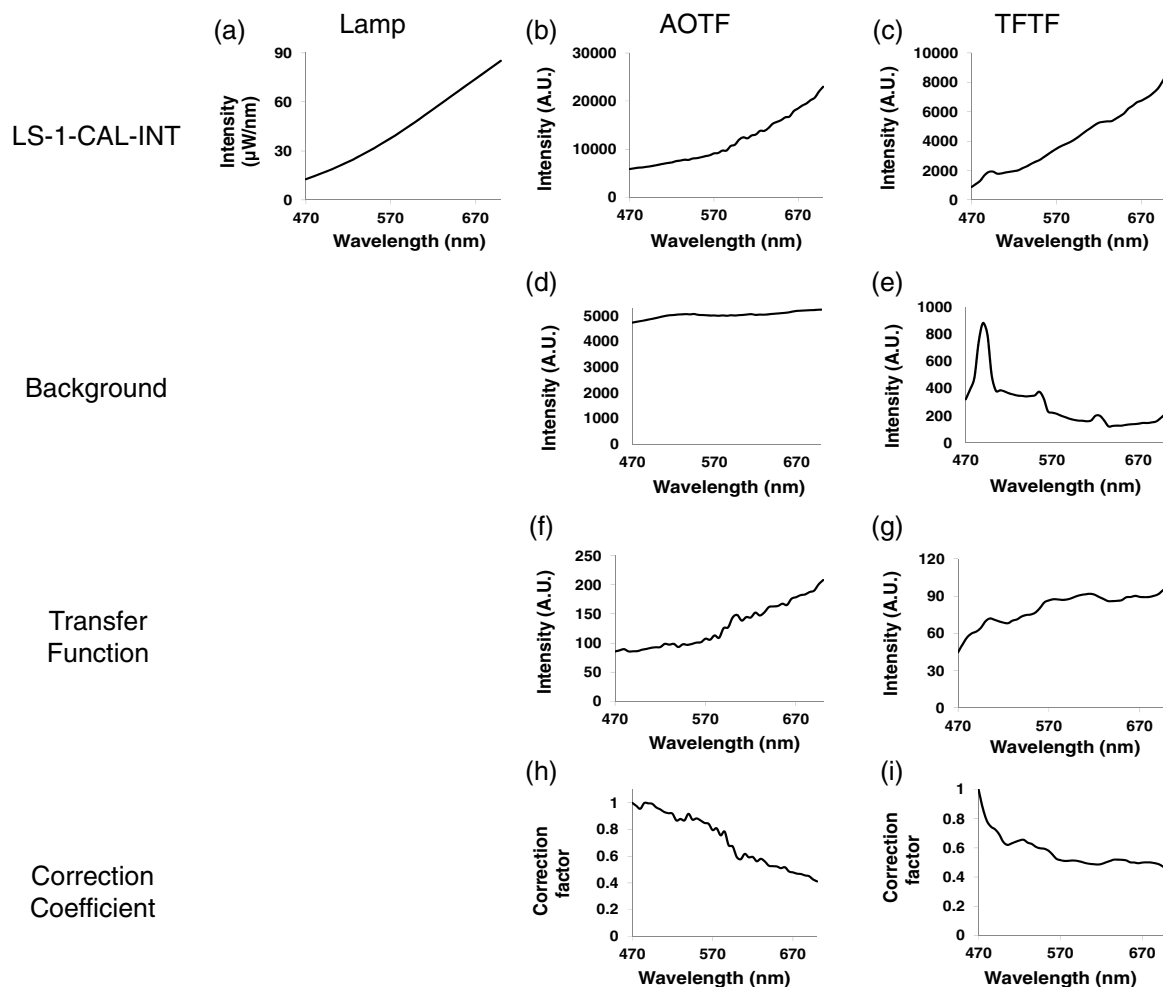


Fig. 4 Flat-field correction for the AOTF and TFTF systems. (a) The National Institute of Science and Technology (NIST)-traceable lamp spectrum. Hyperspectral image data from the NIST-traceable lamp were measured using the AOTF (b) and TFTF (c) systems. The background spectrum was also measured with both the AOTF (d) and TFTF (e) systems. The spectra of the NIST-traceable lamp and the background spectra were used to calculate the spectral transfer function of the AOTF (f) and TFTF (g) systems. A correction coefficient (CC) was calculated as the inverse of the transfer function for the AOTF (h) and TFTF (i) systems.

shown in Fig. 6(a) for the AOTF and Fig. 6(b) for the TFTF. The spectral libraries for the AOTF [Fig. 6(c)] and TFTF [Fig. 6(d)] were used to linearly unmix the hyperspectral image data. The abundance of GFP, Hoechst, and autofluorescence for each respective image was calculated for the AOTF [Figs. 6(e), 6(g), and 6(i)] and TFTF [Figs. 6(f), 6(h), and 6(j)] systems. The TFTF system was able to accurately identify Hoechst-stained nuclei and structural features of the lung autofluorescence.

Linearly unmixed images were merged using NIS Elements software (Fig. 7). Autofluorescence structural features were not as well identified in the AOTF system. The average RMS percent error was calculated from four fields of view within the same sample. The average root-mean-square (RMS) percent error (RMS residual divided by the RMS signal) for the AOTF was $38 \pm 7\%$ and $36 \pm 2\%$ for the TFTF. RMS error images for each field of view are shown in Fig. 8.

4 Discussion

4.1 Hyperspectral Imaging Using a TFTF or AOTF

In this article, we have demonstrated a novel hyperspectral filtering technology using TFTFs. We have previously reported the

use of an AOTF in distinguishing GFP-expressing cells in highly autofluorescent lung tissue.³ Here, we have compared the response of the AOTF to that of the TFTF system to demonstrate the capability of the TFTF system to act as a spectral filter for hyperspectral imaging.

There are several differences between the TFTF and AOTF systems. The AOTF diffracts light due to phonon–photon interactions in a solid crystalline lattice, whereas the TFTF filters light through thin-film interference effects. The AOTF system is tuned to a specific wavelength by adjusting the acoustic frequency applied to the crystal, whereas the TFTF is tuned by mechanically rotating the thin-film filter. The AOTF system has an operating range of 450 to 800 nm, whereas the TFTF system operating range is dictated by the number of sequential filters placed in the system; currently five filters are in place, allowing operation from 400 to 710 nm (see Table 1). Each individual TFTF has an operating range of about 40 to 85 nm. Additional tunable thin-film filters can be added to achieve a broader wavelength range. The AOTF tuning speed is limited by the acoustic velocity in the crystalline lattice and is generally 10 to 20 μ s, whereas the TFTF tuning speed is limited by the optomechanical rotation and is currently 50 to 100 ms for tuning.

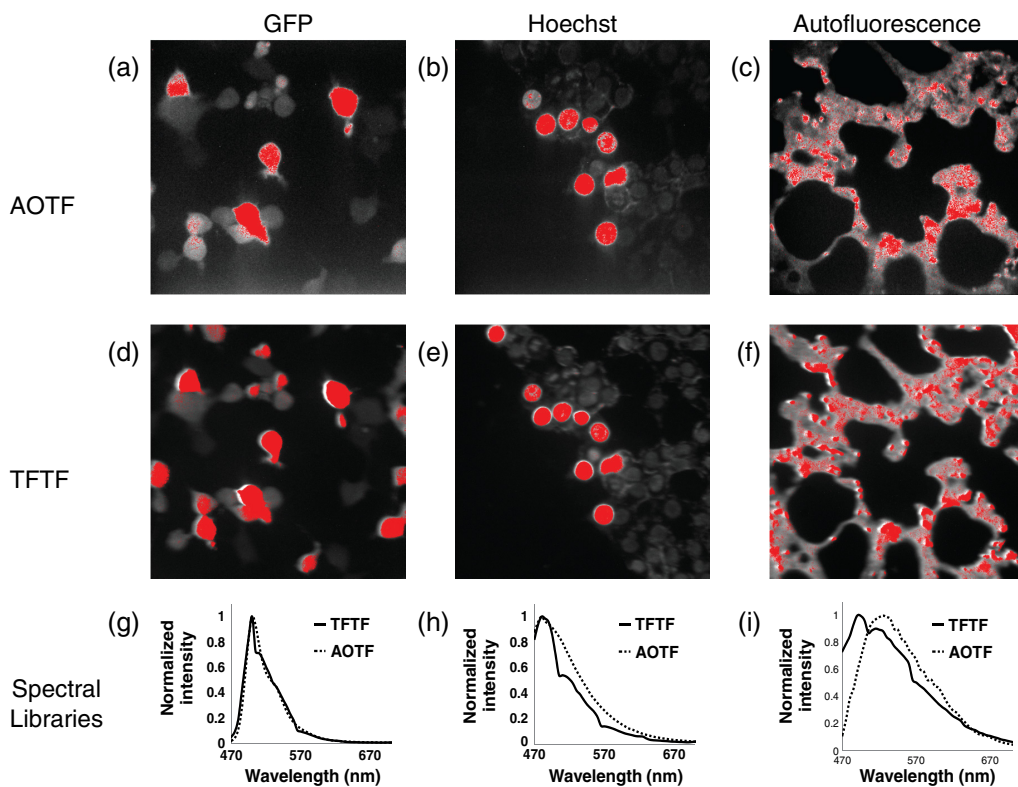


Fig. 5 Control samples for constructing the spectral library. For each sample, then total fluorescence emission (summed across all wavelength bands) is shown as a grayscale image and the region-of-interest (ROI) used to identify the characteristic spectrum for the spectral library is shown in red. Confluent monolayers of highly proliferative pulmonary microvascular endothelial cells (PMVECs) were used for measuring green fluorescent protein (GFP) and Hoechst. A control tissue sample was used to obtain the lung autofluorescence spectrum. GFP, Hoechst, and autofluorescence were measured with the AOTF system (a)–(c) as well as the TFTF system (d)–(f). ROIs (shown in red) were selected by intensity thresholding using ENVi software. The average fluorescence emission spectrum from these regions was measured for GFP (g), Hoechst (h), and lung autofluorescence (i) for the AOTF system (dashed line) and TFTF system (solid line).

sequential wavelengths. In applications where very-fast wavelength switching is not needed, this difference in tuning speeds may be negligible. Additionally, alternative mechanical rotation devices could be employed to greatly increase the wavelength switching speed of the TFTF system. Finally, the cost to construct a fully automated tunable filter system using TFTF technology can be roughly 50% of the price of current, commercially available AOTF systems if constructed using appropriate off-the-shelf electronic and motor components.

4.2 Filter Characterization of the TFTF Identified Higher Light Transmission but Lower Spectral Resolution than the AOTF

To further test the optical specifications of the TFTF compared to the AOTF, we measured the light transmission through each filter system using the microscope lamp as a light source. The TFTF system had a transmission of 90% to 95%, whereas the AOTF had a transmission of 20% to 25%. Additionally, the TFTF system had a higher OD (2.5 to 3.0) than the AOTF (OD of 2.0 to 2.75). Our apparatus permitted only limited evaluation of the OD for both systems due to stray room light and the dynamic range of the USB-coupled spectrometer; however, our data suggests that the TFTF system possesses better out-of-band rejection than the AOTF system (Fig. 9). Theoretically, the TFTF system has a much higher out-of-band blocking power than the AOTF (OD of 5 versus OD of 3). The lower out-of-band rejection

of the AOTF could have resulted in the high level of nonspecific background signal that we observed during flat spectral calibration [Fig. 4(d)]. In applications featuring a weak signal and a strong signal in the same sample, the ability to attenuate out-of-band light is critical. It should also be noted that while the ideal band-pass spectrum of the TFTF system has a flat top, when implemented in a microscope setting, effects of numerical aperture and collimation result in a spectrum with a rounded peak. This is because of the angular dependence of the wavelength of the tunable filters and the compromise that must be made between collimation and preserving a high numerical aperture within the relay optics.

The wavelength calibration and bandwidth of both tunable filter systems were also evaluated using a MIDL. The AOTF produced a small amount of spectral broadening of the narrow emission bands of the MIDL due to its bandwidth (8.5 nm FWHM), whereas the TFTF system produced much more spectral broadening (16 to 20 nm FWHM). As a result, the AOTF would provide improved spectral resolution for distinguishing fluorophores with narrow emission peaks, whereas the TFTF would provide improved signal strength for detecting weak fluorescence emission. It should be noted that the AOTF bandwidth can be adjusted by adjusting the complex waveform applied to the piezoelectric transducer, while in the future, alternative designs of TFTF filters could be manufactured with broader or narrower bandwidths, as required for a specific application. However, future development work would be required to

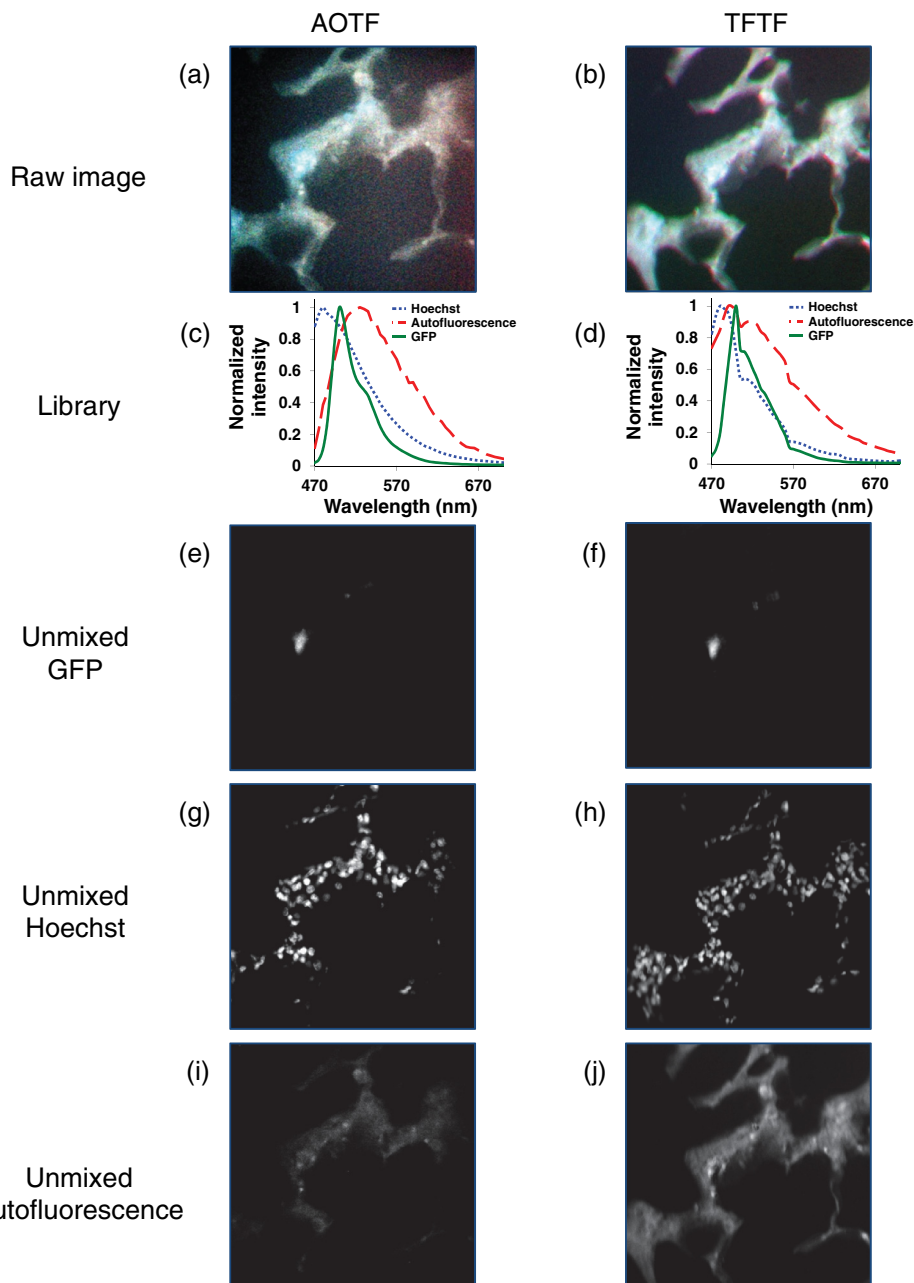


Fig. 6 Samples containing GFP, Hoechst, and lung autofluorescence were imaged with AOTF, (a) and TFTF (b) systems for the same field-of-view. A linear spectral unmixing algorithm was used in conjunction with the spectral library from either the AOTF (c) or TFTF (d). The abundances of GFP (e)–(f), Hoechst (g)–(h), and autofluorescence (i)–(j) were calculated. The average root-mean-square (RMS) percent error (calculated from four fields of view) was $38 \pm 7\%$ for the AOTF and $36 \pm 2\%$ for the TFTF.

ascertain whether a TFTF filter could be designed to match the 8.5-nm bandwidth of the AOTF system.

4.3 Spectral Correction Was Performed and Spectral Libraries Acquired Using Both the AOTF and the TFTF Systems

Each image was corrected for wavelength-dependent attenuation using a previously described spectral correction procedure.³ Differences between the TFTF and AOTF systems were apparent at several wavelengths. Specifically, slight spectral “artifacts” in the TFTF background spectrum could be

identified at 505, 565, and 625 nm. These wavelengths correspond to the mechanical switching between individual thin-film filters (Table 1: Filter 2 to Filter 3, Filter 3 to Filter 4, and Filter 4 to Filter 5). These differences in spectra were also present in the spectral library for the TFTF system. By contrast, the AOTF did not present these artifacts. Improving the variability in bandwidth and transmission when switching between adjacent filters in the TFTF system may reduce the spectral artifacts shown in Figs. 3 and 4. In either case, the representative spectra in the library could be effectively applied to linearly unmix images with a mixture of all signals (as described below).

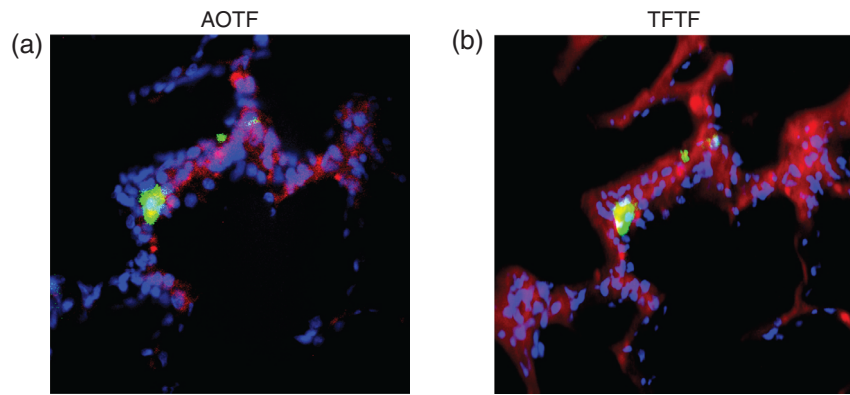


Fig. 7 Unmixed images from the AOTF (a) and TFTF (b) were false colored and merged using Nikon Elements software. Hoechst-stained nuclei were colored blue, GFP-expressing PMVECs were colored green, and tissue autofluorescence was colored red.

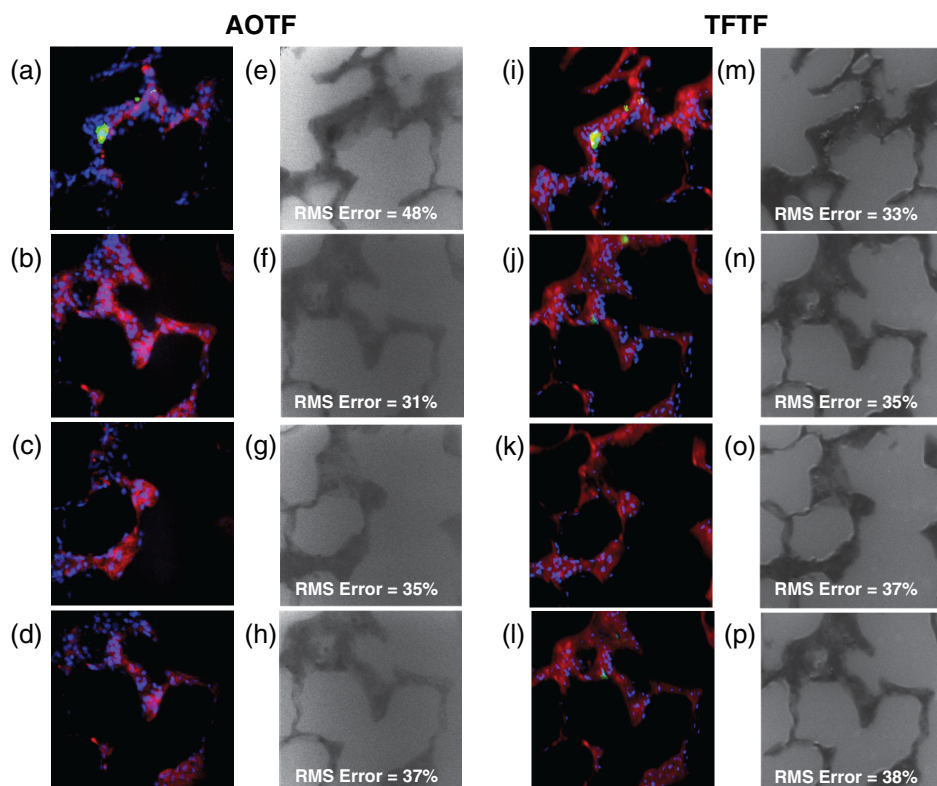


Fig. 8 Merged images and mean error images for each system from four fields of view. Four fields of view were imaged in a 2×2 square on a sample slide. GFP was present in three fields of view [AOTF—(a), (b), (d); TFTF—(i), (j), (l)], however, GFP fluorescence was not visible for the AOTF in images (b) and (d). The AOTF had a higher standard deviation in RMS percent error than the TFTF (AOTF, 7%; TFTF, 2%) and a higher average RMS percent error (AOTF, 38%; TFTF, 36%).

4.4 GFP, Hoechst, and Auto fluorescence Can Be Unmixed and Identified Using Both the AOTF and TFTF Systems

Spectral images (after flat spectral correction) were separated into abundance images for each component using linear spectral unmixing (using ENVI software). Artifacts in the TFTF spectrum (associated with mechanical switching of the filters) did not have a significant effect on the spectral separation of GFP, Hoechst, or auto fluorescence. Results from Figs. 5–7 indicate that the TFTF system is capable of distinguishing multiple fluorophores in auto fluorescent tissue. It is interesting to note

that the spectral artifacts shown in the spectral library (Fig. 5) have little effect on the ability of the TFTF to discriminate GFP from auto fluorescence. This is likely because these same artifacts are present in each image acquired (they are a characteristic of the system). Because linear unmixing minimizes the least square error summed across all wavelength bands, because the square error at each wavelength band is calculated independently, and because the spectral artifact occurs reproducibly at the same band in each spectral image (in both the spectral library and spectral image being unmixed), it is likely that the specific band with the spectral artifact is accurately matched to the artifact in the spectral library and that the magnitude of the resulting

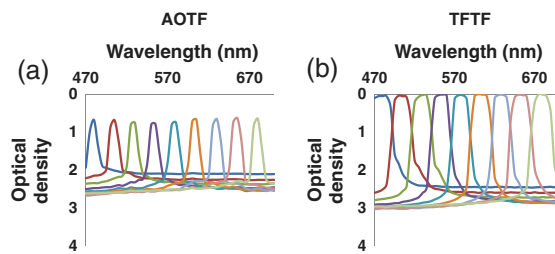


Fig. 9 Optical density plots for the AOTF (a) and TFTF (b) systems. The peaks represent center tuning wavelengths for each spectral filtering system. For the AOTF, the wavelength band was adjusted by adjusting the frequency supplied to the crystal. For the TFTF, the wavelength band was adjusted by either rotating a tunable filter to a desired angle or by switching between the five tunable filters in the filter array (filter-CWL-angle specifications are given at the end of the caption). The AOTF has lower light transmission at the CWLs (0.8 OD) and lower optical density for out-of-band wavelengths (2 to 2.75 OD) than the TFTF. The TFTF has an optical density of 0.03 OD at CWLs and 2.5 to 3.0 OD for out-of-band wavelengths. Hence, the in-band-to-out-of-band OD difference for the AOTF is 1.7 to 2.2 OD, whereas the TFTF is 2.5 to 3.0 OD. TFTF tuning settings for each CWL as listed by CWL, filter model #, angular rotation: (1) 470 nm, TBP01-503-15, 45 deg; (2) 475 nm, TBP01-503-15, 39 deg; (3) 500 nm, TBP01-503-15, 14 deg; (4) 525 nm, TBP01-564-14, 42 deg; (5) 550 nm, TBP01-564-14, 23 deg; (6) 575 nm, TBP01-632-14, 49 deg; (7) 600 nm, TBP01-632-14, 34 deg; (8) 625 nm, TBP01-632-14, 14 deg; (9) 650 nm, TBP01-708-13, 47 deg; (10) 675 nm, TBP01-708-13, 34 deg; (11) 700 nm, TBP01-708-13, 17 deg.

least square error in that wavelength band is largely unaffected by the spectral artifact. Hence, the spectral artifacts noted in the spectral library have little effect on the ability of the TFTF system to distinguish GFP from autofluorescence.

The RMS percent error associated with linear unmixing was also determined for each image (Fig. 8). The RMS percent error was used to identify which features of the image had the largest associated error. In addition, if there were additional fluorescent species in the image that were not accounted for, the RMS percent error image would indicate the regions of unaccounted species as pixels with higher percent error. The overall linear unmixing results indicate that the two filter systems have comparable mean RMS percent errors (AOTF— $38 \pm 7\%$, TFTF— $36 \pm 2\%$). Qualitatively, the TFTF system was able to better define nuclei, GFP-expressing PMVECs, and autofluorescence, although these differences may be due to differences in detectors as well as the tunable filters themselves.

5 Conclusions

Hyperspectral fluorescence microscopy has become a valuable tool for quantitative cellular and tissue imaging. In this work, we have demonstrated a novel tunable filter system for hyperspectral imaging, the TFTF. We have compared this system to a standard tunable filter technology, an AOTF. Images from both the TFTF and the AOTF were used to accurately distinguish GFP from autofluorescence in prepared lung tissue slices. Hoechst was also used to enable identification of nuclei as a reference for tissue morphology. The TFTF system provided a higher percentage transmission and out-of-band blocking power, whereas the AOTF system provided a narrower bandwidth and faster wavelength switching speed. Hence, the TFTF system presents an alternative tunable filter technology that is well suited for measuring weak fluorescence signals where very high speed is not needed. In future work, the TFTF system could be

expanded to allow tuning of both the CWL and bandwidth at higher wavelength-switching speeds.

Acknowledgments

The authors would like to acknowledge support from NIH grant P01 HL066299, the Alabama Space Grant Consortium, and the ISAC Scholar's Program. VersaChrome filters and tuning hardware for this study were provided by Semrock, Inc., a Unit of IDEX.

References

1. S. Leavesley et al., "An excitation wavelength-scanning spectral imaging system for preclinical imaging," *Rev. Sci. Instrum.* **79**(2), 023707 (2008).
2. T. Vo-Dihn et al., "A hyperspectral imaging system for in vivo optical diagnostics," *IEEE Eng. Med. Biol. Mag.* **23**(5), 40–49 (2004).
3. S. Leavesley et al., "Hyperspectral imaging microscopy for identification and quantitative analysis of fluorescently labeled cells in highly autofluorescent tissue," *J. Biophoton.* **5**(1), 67–84 (2012).
4. R. Lansford, G. Bearman, and S. E. Fraser, "Resolution of multiple green fluorescent protein color variants and dyes using two-photon microscopy and imaging spectroscopy," *J. Biomed. Opt.* **6**(3), 311–318 (2001).
5. M. Han et al., "Quantum-dot-tagged microbeads for multiplexed optical coding of biomolecules," *Nat. Biotechnol.* **19**(7), 631–635 (2001).
6. R. M. Zucker et al., "Reliability of confocal microscopy spectral imaging systems: use of multispectral beads," *Cytom. Part A* **71**A(3), 174–189 (2007).
7. N. Gupta, "Acousto-optic-tunable-filter-based spectropolarimetric imagers for medical diagnostic applications—instrument design point of view," *J. Biomed. Opt.* **10**(5), 051802 (2005).
8. G. C. Tang et al., "Ultraviolet-visible acousto-optic tunable spectroscopic imager for medical diagnosis," *J. Biomed. Opt.* **3**(1), 80–84 (1998).
9. S. Lam et al., "Localization of bronchial intraepithelial neoplastic lesions by fluorescence bronchoscopy," *Chest* **113**(3), 696–702 (1998).
10. Y. L. Yang et al., "Characteristic autofluorescence for cancer diagnosis and its origin," *Lasers Surg. Med.* **7**(6), 528–532 (1987).
11. C. Chang, D. Sud, and M. Mycek, "Fluorescence lifetime imaging microscopy," *Methods Cell Biology*, Vol. 81, pp. 495–524 (2007).
12. H. C. Gerritsen et al., "Fluorescence lifetime imaging in scanning microscopes: acquisition speed, photon economy and lifetime resolution," *J. Microsc.* **206**(3), 218–224 (2002).
13. Y. Sun, R. N. Day, and A. Periasamy, "Investigating protein-protein interactions in living cells using fluorescence lifetime imaging microscopy," *Nat. Protoc.* **6**(9), 1324–1340 (2011).
14. K. Suhling et al., "Imaging the environment of green fluorescent protein," *Biophys. J.* **83**(6), 3589–3595 (2002).
15. A. T. Harris, "Spectral mapping tools from the earth sciences applied to spectral microscopy data," *Cytom. Part A* **69**A(8), 872–879 (2006).
16. J. M. Lerner, N. Gat, and E. Wachman, "Approaches to spectral imaging hardware," *Curr. Protoc. Cytom.* **53**(12.20), 12.20.1–12.20.40 (2010).
17. J. R. Mansfield et al., "Autofluorescence removal, multiplexing, and automated analysis methods for in-vivo fluorescence imaging," *J. Biomed. Opt.* **10**(4), 041207 (2005).
18. Y. Gu et al., "Quantitative fluorescence resonance energy transfer (FRET) measurement with acceptor photobleaching and spectral unmixing," *J. Microsc.* **215**(2), 162–173 (2004).
19. C. Thaler and S. S. Vogel, "Quantitative linear unmixing of CFP and YFP from spectral images acquired with two-photon excitation," *Cytom. Part A* **69**A(8), 904–911 (2006).
20. S. J. Leavesley et al., "Assessing FRET using spectral techniques," *Cytom. A Early View* (2013).
21. T. Zimmermann, J. Riedorf, and R. Pepperkok, "Spectral imaging and its applications in live cell microscopy," *FEBS Lett.* **546**(1), 87–92 (2003).
22. Y. Hiraoka, T. Shimi, and T. Haraguchi, "Multispectral imaging fluorescence microscopy for living cells," *Cell Struct. Funct.* **27**(5), 367–374 (2002).
23. J. N. Meyer et al., "Intracellular uptake and associated toxicity of silver nanoparticles in *Caenorhabditis elegans*," *Aquat. Toxicol.* **100**(2), 140–150 (2010).

24. R. A. Schultz et al., "Hyperspectral imaging: a novel approach for microscopic analysis," *Cytometry* **43**(4), 239–247 (2001).
25. D. T. Dicker and J. Lerner, "Differentiation of normal skin and melanoma using high resolution hyperspectral imaging," *Cancer Biol. Ther.* **5**(8), 1033–1038 (2006).
26. D. T. Dicker, J. M. Lerner, and W. S. El-Deiry, "Hyperspectral image analysis of live cells in various cell cycle stages," *Cell Cycle* **6**(20), 2563–2570 (2007).
27. D. N. Stratis et al., "Comparison of acousto-optic and liquid crystal tunable filters for laser-induced breakdown spectroscopy," *Appl. Spectrosc.* **55**(8), 999–1004 (2001).
28. E. S. Wachman et al., "AOTF microscope for imaging with increased speed and spectral versatility," *Biophys. J.* **73**(3), 1215–1222 (1997).
29. Y. Garini, I. T. Young, and G. McNamara, "Spectral imaging: principles and applications," *Cytom. Part A* **69**A(8), 735–747 (2006).
30. J. Vila-Francés et al., "Configurable-bandwidth imaging spectrometer based on an acousto-optic tunable filter," *Rev. Sci. Instrum.* **77**(7), 073108 (2006).
31. P. K. Tien, "Light waves in thin films, and integrated optics," *Appl. Opt.* **10**(11), 2395–2413 (1971).
32. J. King et al., "Structural and functional characteristics of lung macro- and microvascular endothelial cell phenotypes," *Microvasc. Res.* **67**(2), 139–151 (2004).
33. T. Erdogan, "Optical filters for wavelength selection in fluorescence instrumentation," *Curr. Protoc. Cytom.*, **56**(2.4), 2.4.1–2.4.25 (2011).